Mapping microbubble viscosity using fluorescence lifetime imaging of molecular rotors

Neveen A. Hosny[a], Graciela Mohamedi[b], Paul Rademeyer[b], Joshua Owen[b], Yilei Wu[a], Meng-Xing Tang[c], Robert J. Eckersley[d,e], Eleanor Stride[b,1], and Marina K. Kuimova[a,1]

Departments of [a]Chemistry and [c]Bioengineering, Imperial College London, London SW7 2AZ, United Kingdom; [b]Department of Engineering Science, Institute of Biomedical Engineering, University of Oxford, Oxford OX3 7DQ, United Kingdom; [d]Biomedical Engineering Department, Division of Imaging Sciences, King's College London, London SE1 7EH, United Kingdom; and [e]The Rayne Institute, St Thomas' Hospital, London SE1 7EH, United Kingdom

Edited by David A. Weitz, Harvard University, Cambridge, MA, and approved April 23, 2013 (received for review January 23, 2013)

Encapsulated microbubbles are well established as highly effective contrast agents for ultrasound imaging. There remain, however, some significant challenges to fully realize the potential of microbubbles in advanced applications such as perfusion mapping, targeted drug delivery, and gene therapy. A key requirement is accurate characterization of the viscoelastic surface properties of the microbubbles, but methods for independent, nondestructive quantification and mapping of these properties are currently lacking. We present here a strategy for performing these measurements that uses a small fluorophore termed a "molecular rotor" embedded in the microbubble surface, whose fluorescence lifetime is directly related to the viscosity of its surroundings. We apply fluorescence lifetime imaging to show that shell viscosities vary widely across the population of the microbubbles and are influenced by the shell composition and the manufacturing process. We also demonstrate that heterogeneous viscosity distributions exist within individual microbubble shells even with a single surfactant component.

FLIM | microviscosity

The potential utility of surfactant stabilized microbubbles (Fig. S1*A*) as contrast agents for ultrasound and more recently multimodality imaging combined with therapeutic delivery has made them the subject of intensive study (1). A wide variety of experimental techniques and theoretical modeling have been applied to characterize their behavior and manufacturing techniques developed to provide improved control over their properties (Fig. S1*B*). The surfactant coating not only stabilizes bubbles against diffusion of encapsulated gases, it can also be used to functionalize the bubble surface for a given application; for example, it can provide a scaffold to which targeting molecules or drugs are attached. Importantly, its properties can also be selected to "tune" the response of a microbubble to ultrasound (2). The exact role of the physicochemical parameters of the coating, however, is still not fully understood, and they are known to vary considerably across a microbubble population (3).

Currently, only indirect and quasistatic methods exist to measure the viscoelastic properties of the microbubble coating. These include micropipette aspiration (4), ultrasound scattering and attenuation measurements (5), fluorescence recovery after photobleaching (6), and atomic force microscopy (7). Estimates have also been successfully obtained through fitting theoretical models to acoustic and/or high-speed camera measurements of single microbubbles (8). Importantly, this requires the microbubble coatings to be treated as a continuum (6), including coatings of mixed compositions—for example, phospholipids and emulsifiers (9). There is now firm evidence from numerous studies—for example, by transmission electron microscopy (TEM) and fluorescence imaging (10, 11)—that partitioning and domain formation occurs in multicomponent bubble shells. These domains govern the surface microstructure (12) and affect the viscoelastic properties of the microbubble shell and hence their functional behavior.

To address these problems, we have adopted an alternative strategy, using a detection method that allows not only the effective viscosity of microbubble coatings to be quantified but also any spatial variations to be precisely mapped. Our method applies fluorescence lifetime imaging microscopy (FLIM) (13) to exploit the viscosity-sensitive photophysical properties of a "molecular rotor," the mesosubstituted 4,4-difluoro-4-bora-3a,4a-diaza-s-indacene (BODIPY-C_{10}) (Fig. 1). This fluorescent dye can be seamlessly incorporated into structures such as a surfactant coating (Fig. S1*C*), in this case in the "tail" region of the phospholipid layer surrounding a microbubble. Since it is not a "tag" that is directly bound to the surfactant molecules, it does not affect their behavior (Fig. S3). BODIPY-C_{10} behaves as a molecular rotor, due to the rotation of the phenyl ring in and out of the plane of the BODIPY chromophore (Fig. 1). As a result of this rotation, the nonradiative decay pathways are activated, leading to a reduction in the fluorescence quantum yield and the lifetime of the rotor compared with that in a viscous environment (14).

For the purposes of microbubble imaging, we elected to use fluorescence lifetime to detect viscosity. Unlike fluorescence intensity, which changes as a function of the dye concentration, the fluorescence lifetime can provide a viscosity measure that is not affected by inhomogeneous distribution of the rotor in a given region of the bubble coating. We experimentally determined the relationship between the fluorescence lifetime and viscosity for BODIPY-C_{10} for a wide range of viscosities [0.6–1140 centipoise (CP)] (Fig. 1*A*), and this was found to be well described by the Förster–Hoffmann equation (15) (Eqs **1–4**). This provided the means to produce a calibration graph (Fig. 1*B*) for converting lifetime into a quantitative measure of viscosity. FLIM can detect individual lifetimes with the spatial resolution of a multiphoton microscope (*ca.* 200 nm). Thus, FLIM of the molecular rotor BODIPY-C_{10} provides a minimally invasive technique that can directly quantify and image viscosity at a macro- or microscopic resolution from lipid membranes of individual microbubbles. Importantly, the rate of intramolecular rotation in BODIPY-C_{10} also corresponds to bubble oscillations at ultrasonic frequencies. It thus provides a more relevant measure than quasistatic measurements and has the potential to be used during ultrasound exposure, to determine also how coating properties may vary during bubble oscillation; although this was not exploited specifically in this study.

In this study, we investigate the impact of the microbubble preparation method, coating composition, and size on the magnitude and spatial distribution of the effective surface viscosity of

Author contributions: E.S. and M.K.K. designed research; N.A.H., G.M., P.R., J.O., and Y.W. performed research; M.-X.T. and R.J.E. contributed new reagents/analytic tools; N.A.H., G.M., and P.R. analyzed data; and N.A.H., E.S., and M.K.K. wrote the paper.

The authors declare no conflict of interest.

This article is a PNAS Direct Submission.

[1]To whom correspondence may be addressed. E-mail: m.kuimova@imperial.ac.uk or eleanor.stride@eng.ox.ac.uk.

This article contains supporting information online at www.pnas.org/lookup/suppl/doi:10.1073/pnas.1301479110/-/DCSupplemental.

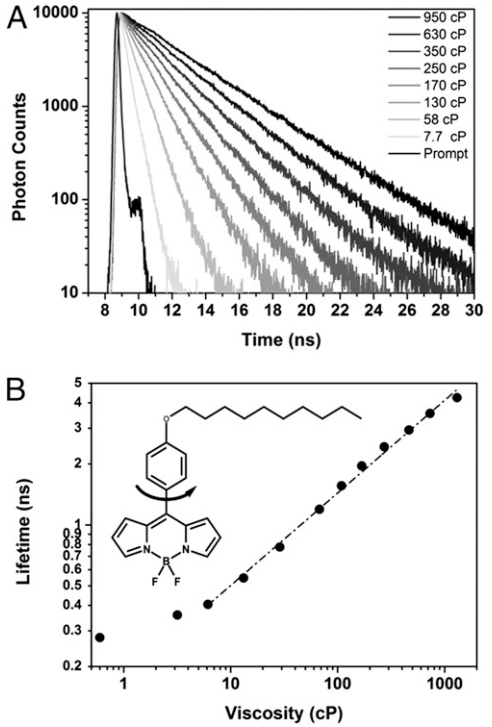

Fig. 1. BODIPY-C_{10} fluorescence lifetime calibration vs. viscosity. (*A*) Selected fluorescence decay traces recorded in methanol/glycerol mixtures (30–95% glycerol) of different viscosity. (*B*) The logarithmic calibration plot of measured lifetimes vs. viscosity plotted according to the Förster–Hoffmann equation, which was fitted with a linear fit (dash-dot line) and found to be linear between 7.7 and 1,140 cP. Chemical structure of BODIPY-C_{10} is also shown.

individual bubbles, and compare this with the variation in their response to ultrasound excitation.

Results and Discussion

Global Microbubble Analysis. Initially, we used a single phospholipid 1,2-Distearoyl-sn-glycero-3-phophocholine (DSPC) to prepare microbubbles using both a conventional sonication method and a microfluidic "T"-junction device. The latter enables the preparation of bubbles with a high degree of control over their size and uniformity, while the former produces bubbles with a broad size distribution. The sonication method has the advantage of producing bubbles in high yield and also with superior stability. However, the underlying reasons for the difference in stability are not fully understood. By applying the molecular rotors approach, we were able to determine the mean viscosity of T-junction microbubbles as 663 ± 119 cP (3.40 ± 0.26 ns), which was found to be significantly lower than for the sonicated bubble population at 857 ± 110 cP (3.83 ± 0.22 ns) (Fig. 2*A*). This is consistent with lower diffusivity and hence the greater stability of the sonicated microbubbles. This is an instance of the direct physical characterization of the effect of preparation method upon microbubble structure, which could explain the differences in their behavior.

The composition of the microbubble coating is known to significantly affect both the stability and response of microbubbles to ultrasound (12). We compared fluorescence lifetimes detected from microbubbles produced by sonication from lipid-dye films containing DSPC, L-alpha-Phosphatidylcholine (L-alpha PC), and DSPC+PEG in different ratios (*Materials and Methods* and *SI Materials and Methods*). The DSPC and L-alpha PC microbubbles were found to exhibit a similar range of viscosities (Fig. 2*B*) as might be expected given the similarity in their molecular structure (Fig. S9). The addition of PEG to DSPC, however, had a marked effect, with viscosity being significantly reduced with increasing PEG ratio: PEG 1:1 DSPC 337 ± 57 cP (2.49 ± 0.2 ns), PEG 1:4 DSPC 426 ± 57 cP (2.78 ± 0.2 ns), and PEG 1:9 DSPC 506 ± 73.9 cP (3.01 ± 0.21 ns) (Fig. 2*C*). For all compositions, comparison of the observed lifetime for microbubbles of different size indicated that there was no statistically significant correlation between shell viscosity and microbubble size (Fig. S4).

There was, however, considerable variation across each population in the measured viscosity for all shell compositions (Fig. 2). This large viscosity variation was reflected in the ultrasound measurements. The mean power of the scattered pressure detected from individual bubbles decreased with increasing proportion of PEG in the coating, corresponding to a reduction in the measured viscosity as would be predicted (Fig. 2*D*). There was, however, a very large SD in the measurements even though the bubble size distributions were matched between the different compositions and batches (Fig. 2 and Fig. S5). Theoretical simulations (Fig. 2*D*) further indicated that the scattered pressure is also sensitive to variations in effective elasticity of the microbubble coating, and

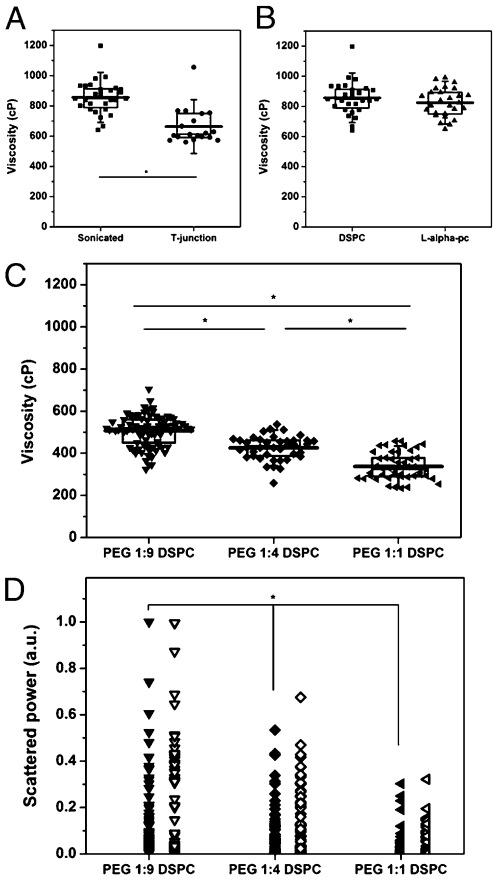

Fig. 2. Quantification of microbubble shell viscosities. (*A*) Viscosity dependence on microbubble manufacturing method as measured by BODIPY-C_{10} lifetime, comparing sonication (■) ($n = 28$) to T-junction preparation (●) ($n = 19$) (*$P < 0.001$). (*B*) Effect of microbubble lipid composition on viscosity for DSPC (■) ($n = 28$), L-alpha-PC (△) ($n = 27$). (*C*) Viscosity dependence on microbubble coat composition: PEG 1:9 DSPC (▽) ($n = 82$), PEG 1:4 DSPC (◆) ($n = 41$), and PEG 1:1 DSPC (◄) ($n = 46$). Boxes show 25–75% of microbubbles, whiskers are the SD, and thick bar indicates the mean value (*$P < 0.001$). (*D*) Normalized scattered power at the fundamental frequency (2.25 MHz) for ratios of PEG 1:9 DSPC, PEG 1:4 DSPC, and PEG 1:1 DSPC ($n = 150$, 80, and 69) (*$\chi^2 < 0.05$) are compared between experiment (closed symbol) and simulations (open symbol) using a modified Rayleigh–Plesset equation. The simulations use an elastic modulus and viscosity, respectively, of 70 MPa and 507 cP (1:9), 40 MPa and 426 cP (1:4), and 10 MPa and 337 cP (1:1).

this would be expected to vary with composition as well as viscosity. This reinforces the need for independent methods for determining coating characteristics such as that presented in this study.

Individual Microbubble Analysis. A significant advantage of the molecular-rotor–based viscosity determination is the possibility of spatially resolved viscosity imaging. To further examine the differences between bubbles within a single population, we determined the fluorescent lifetimes in each pixel of individual DSPC microbubble images (Fig. 3). Fig. 3*A* shows two bubbles of a similar size, but with different lifetime distributions, as identified by two separate Gaussian peaks in the lifetime histogram (Fig. 3*B*). We applied a seismic color palette to the lifetime histogram (assigned a single color to each lifetime peak), which clearly differentiated the two Gaussian distributions. This operation confirmed that the lifetimes in each peak originated from the two separate bubbles, which could be assigned viscosities of 600 ± 140 cP (3.26 ± 0.33 ns) and 1,112 ± 191 cP (4.32 ± 0.33 ns) according to the calibration graph (Fig. 1*B*).

In addition, we produced lifetime maps over the surface of single bubbles. Even though the lifetime decay was found to be monoexponential in every pixel, significantly different viscosities were observed across the same bubble (Fig. 3*C*). For example, in Fig. 3*D*, we resolved the average lifetimes in two separate regions of the same bubble, A = 3.43 ± 0.11 ns and B = 3.63 ± 0.11 ns, corresponding to viscosity differences of 670 ± 50 cP and 761 ± 54 cP, respectively (see Fig. S6 for further analysis). These data clearly demonstrate that even within a single bubble made up of a pure DSPC lipid, vastly heterogeneous viscosity distribution could be observed. Our experiments were conducted at an ambient temperature that was much lower than the gel transition temperature of DSPC (55 °C), and lack of membrane fluidity may be partly responsible for this inhomogeneity. In addition, the regions of higher apparent viscosity may correspond to regions of lamellae within the coating. These observations confirm that microbubbles should not be modeled as having a continuous shell, even for single lipid component systems.

The same methodology could be applied to determine the effects of interactions between bubbles on the surface characteristics (Fig. 4*A*). In Fig. 4*B* we used the TRI2 lifetime software (16) to extract and analyze the histogram information from individual bubbles in contact with their neighbors. As a collective for all of the bubbles in the field of view, the histogram (Fig. 4*B*, gray line) shows no distinguishing features. However, when each bubble's histogram was individually analyzed, distinct subsections could be easily identified and associated to each bubble. It was also clear that each histogram in Fig. 4*B* had a non-Gaussian shape, unlike the two bubbles in Fig. 3*B*. The lack of symmetry suggested a nonhomogeneous viscosity distribution similar to that observed in Fig. 3*D* (Fig. S6). We have applied the peak fitting analysis to the individual histograms of bubbles 2 and 3 in Fig. 4 and identified that there are essentially two lifetime populations with a broad intersection range between 3.1 ns and 3.4 ns (Fig. S7). Using this crossover band to differentiate areas of low and high viscosity, we applied a seismic color plot to all bubbles. It can be clearly seen that bubble areas in contact with the neighboring bubbles appear as blue (lower viscosity, lifetimes below 3.1 ns), while areas of bubbles that are contact free are red (higher viscosity, lifetimes above 3.4 ns). Visual inspection of the image suggests that bubble contact lowers viscosity. Changes in refractive index due to contact would not be sufficient to account for these differences. Potentially, formation of bilayer/multilamellar structures with lower viscosities in the contact region (14) or shielding of the lipid phosphate groups from the surrounding water could be responsible, although further work is required to verify these hypotheses. These observations have practical implications for microbubble applications in vivo where they are initially subject to contact during injection at high concentration in bolus form ~10^9 bubbles per mL and subsequently from other structures formed from lipidic materials (e.g., plasma membranes of endothelial cells). Currently, these interactions are poorly understood and not accounted for in theoretical models.

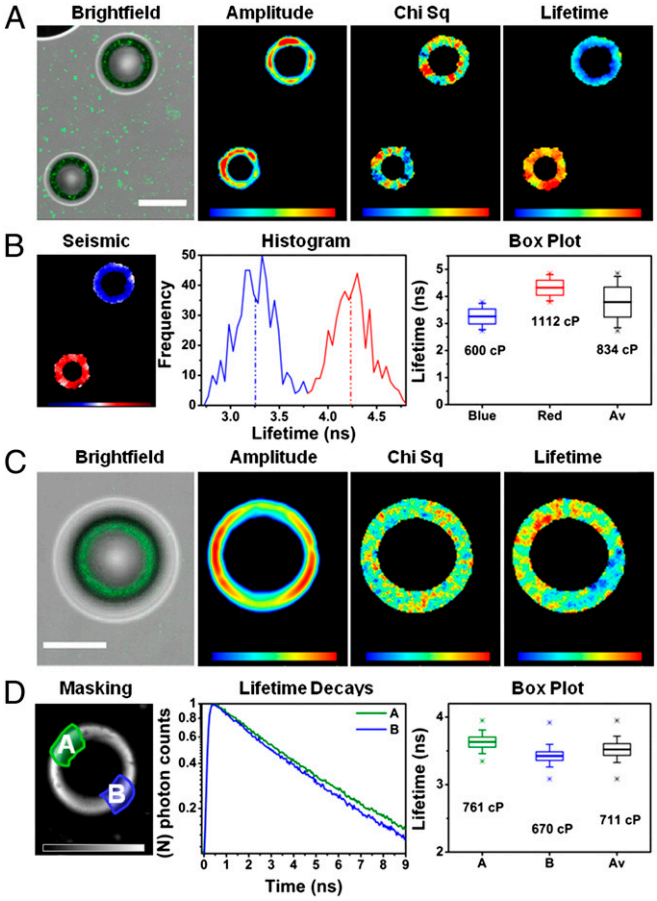

Fig. 3. In-depth individual microbubble analysis. (*A*) Brightfield overlaid with confocal fluorescence images of two individual DSPC microbubbles of a similar size containing BODIPY-C_{10}. (Scale bar, 20 μm.) Also shown are the results of FLIM data analysis: fluorescence intensity (amplitude), χ^2 (goodness of fit, χ_r^2 = 0.8–1.2), and lifetime distribution (τ = 2.5–5 ns). (*B*) Analyzing lifetime histogram from bubbles in *A* shows two distinct peaks with maxima at 3.25 ns and 4.2 ns. Applying a seismic color hue midpoint at 3.75 ns identifies that short (blue) and long (red) lifetimes are originating from the two different microbubbles. The lifetime distributions and viscosities for each bubble and the whole image are shown on a box plot. (*C*) Individual microbubble with heterogeneous lifetime morphology across the shell. Same displayed information as in *A* (χ_r^2 = 0.8–1.2, τ = 3–4 ns). (Scale bar, 20 μm.) (*D*) Masking of high lifetime variation zones A (green) and B (blue) from the lifetime image (*C*) allows lifetime/viscosity determination in each area. Separately binning all pixels in zones A and B identifies two clearly distinct monoexponential decays, as shown. The analysis of each decay along with the whole image is shown on a box plot.

Conclusion

We have shown that viscosity mapping using molecular rotor fluorescence lifetime imaging provides a direct means of quantifying the spatial distribution of viscosity in the microbubble coating. We have confirmed that inclusion of the dye within the lipid shell produced no observable effects on the measured viscosity (Figs. S3 and S8) or surface tension (Fig. S8) and that the bubbles were unaffected by irradiation at low laser powers, sufficient to obtain FLIM images (Movies S1 and S2). We have applied this technique to examine the effects of varying

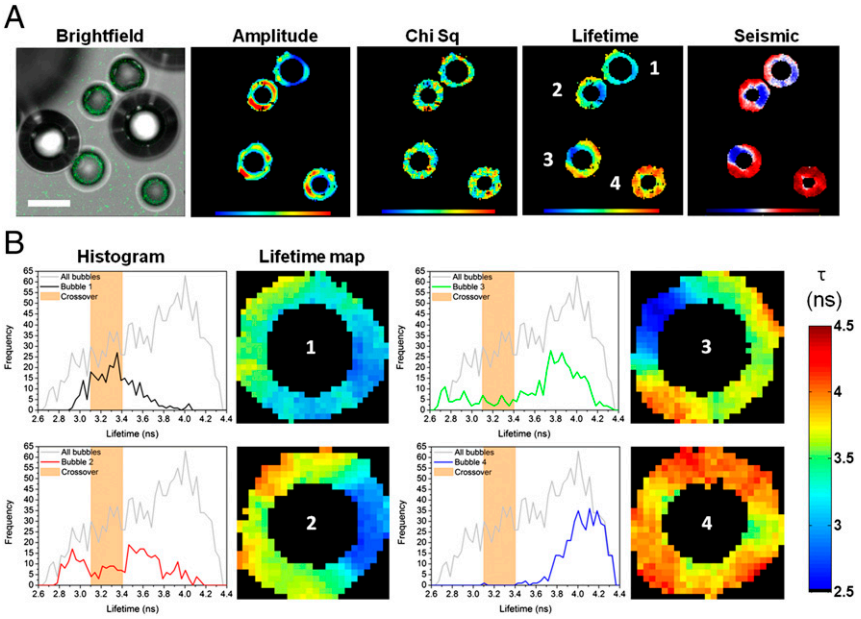

Fig. 4. Investigation of microbubble interactions. (*A*) Brightfield overlaid with confocal fluorescence images of multiple touching DSPC microbubbles containing BODIPY-C_{10}. (Scale bar, 20 μm.) Also shown are the results of FLIM data analysis: fluorescence intensity (amplitude), χ^2 (goodness of fit, χ_r^2 0.8–1.2), and lifetime distribution (τ = 2.6–4.4 ns). Lifetime map with seismic color hue centrally located between 3.1 and 3.4 ns. (*B*) Lifetime histograms and zoomed in FLIM images of the individual masked microbubbles. Individual histograms of four bubbles (black, red, green, and blue) are displayed against histogram of all lifetimes in the image (gray). The rainbow legend on far right represents lifetime variation in the individual lifetime microbubble images. The orange band represents a border region between bubble regions with and without contacts, which is also shown as a white strip in the seismic image in *A*.

composition and production methodologies upon microbubble coating properties. The results have provided direct evidence that there can be a large variation in viscosity across a microbubble population, independent of individual bubble size, and that is correlated to the variability measured in their ultrasound response. We have also demonstrated that varying the coating composition can significantly alter the viscosity, in this case reducing it by the addition of a surfactant (PEG40-stearate). Again this was in agreement with the measured acoustic response of the microbubbles.

We believe that molecular rotors coupled with FLIM provide a unique tool for understanding the structure and physical properties of microbubble coatings at the microscopic scale. This type of data can provide invaluable information for characterizing and predicting microbubble behavior, removing the need for many simplifying assumptions (e.g., shell homogeneity or indirect measurements involving the fitting of several interdependent parameters to a single dataset). Practically, this method provides direct feedback for optimizing microbubble composition and manufacturing processes and, in the future, for accurately determining the effects of time, temperature, bubble concentration, the properties of the surrounding medium, and ultrasound exposure on microbubble characteristics. It may also offer a powerful method for investigating the interaction between microbubbles and biological structures under ultrasound excitation.

Materials and Methods

Viscosity Calibration of Fluorescence Lifetime of BODIPY-C_{10}. Spectroscopic grade methanol–glycerol mixtures were prepared at 12 concentrations between 0% and 100% (vol/vol) glycerol and maintained at room temperature. The dynamic viscosity (η) of each binary mixture was measured using a Stabinger viscometer (SVM 3000, Anton Paar) with an accuracy and precision of ±0.35% and ±0.1%, respectively. BODIPY-C_{10} was dissolved at a concentration of 2.5 μM in the MeOH–glycerol mixtures, and fluorescence decay traces (Fig. 1*A*) were recorded in quartz cuvettes on a time-correlated single photon counting (TCSPC) Jobin Yvon IBH data station (5000F, HORBIA Scientific Ltd.). Samples were excited at 467 nm using a 1 MHz pulsed NanoLED (*N*-467, HORBIA Scientific Ltd.) with a pulse width of 200 ps and a detector monochromator set to 515 ± 5 nm. Decays in all instances were recorded until peak counts were >10,000 counts and at a maintained temperature of 22 °C using a thermostatic circulating chiller (RE104, Lauda Technology Ltd.). The solution viscosity was correlated to the decay traces using the modified form of the Förster–Hoffmann equation. Eq. **1** describes the relationship between quantum yield (Φ_f) and viscosity (η), where z and α represent constants. The quantum yield of a fluorophore can be related to the fluorescence lifetime (τ_f) by the radiative (k_r) and nonradiative rates (k_{nr}), as in Eq. **2**:

$$\Phi_f = z\eta^{\alpha}, \quad [1]$$

$$\Phi_f = \frac{k_r}{k_r + k_{nr}} = \tau_f k_r. \quad [2]$$

Substitution of Eq. **2** into Eq. **1** defines the relationship between the lifetime and viscosity (Eq. **3**):

$$\tau_f = \frac{z\eta^{\alpha}}{k_r}. \quad [3]$$

For calibration purposes it is useful to present this equation in the logarithmic form (Eq. **4**):

$$\log\ \tau_f = \alpha\ \log\ \eta + \text{const}. \quad [4]$$

We observed a linear relationship between (log τ_f) and (log η) in a large viscosity range 7.7–1,140 cP. This calibration plot (Fig. 1*B*) allows the conversion of experimentally measured lifetime (including those from microscopy FLIM experiments) to viscosity. It is important to note that the nature of the viscosity in membranes as measured by molecular rotors is not as straightforward as for bulk samples. At present the precise correlation to conventional measures (i.e., shear or dilatational) of membrane viscosity is not entirely clear (17). The range of action of the molecular rotor is such that the lengthscale on which the viscosity is measured is that of the molecule itself. Glycerol–methanol solutions provide a convenient means of determining the functional relationship between the fluorescence lifetime and viscous nature of the surrounding medium and have been widely used in previous studies using molecular rotors for membrane characterization. This does implicitly assume, however, that the "macroscopic" 3D shear viscosity of the solutions as measured by other means is proportional to the dissipative

mechanisms on the scale of the rotor. We believe this to be a reasonable assumption but are keen to highlight the distinction.

Microbubble Sample Preparation. Stock solutions of Boron-dipyrromethene (BODIPY-C_{10}), DSPC (850365P, Avanti Polar Lipids Inc.),and L-alpha-PC (P4139, Sigma-Aldrich Ltd.) (see Fig. S9 for lipid structures) were prepared in chloroform to concentrations of 4.2 mM, 75.9 mM, and 60 g/L (approx. 76 mM, estimated given unknown precise molecular mass), respectively. A stock solution of Polyoxyethylene(40) stearate (PEG) (P3440, Sigma-Aldrich Ltd.) was prepared in distilled water (24.45 mM). Lipid–dye films (900:1 molar ratio) were prepared by mixing the chloroform stock solutions of a corresponding lipid and BODIPY-C_{10} followed by solvent evaporation. Following this, 2 mL of aqueous solution, of either distilled H_2O or PEG stock solution in water, was added to create a final dye concentration of 4.2 μM. Microbubble samples were prepared from one of five compositions: DSPC, L-alpha-PC, PEG 1:9 DSPC, PEG 1:4 DSPC, and PEG 1:1 DSPC, and two manufacturing procedures. The two methods of microbubble production (*SI Materials and Methods*) were used for this study: sonication and microfluidic T-junction. Both methods required dried lipid–dye films before processing, prepared as described above.

Sonication involved pipetting 2 mL of aqueous solution on top of dried films in glass vials and probe sonication at 6 W for 30 s (XL-2000, Qsonica LLC; probe tip CML-4) followed by mechanical shaking for 30 s to form microbubbles.

T-junction microbubble preparation required a final working volume of 5–7 mL of aqueous solution to be added to the dried films. Before loading in the syringe driver (PHD 4400, Harvard Apparatus), the lipid–dye aqueous solution was bath sonicated to ensure homogenous dispersion of the lipid–dye mixture. A syringe driver forced the lipid–dye aqueous solution at a flow rate of 0.4 mL/min into the specially designed microfluidic polymethylmethacrylate block (18), while simultaneously flowing nitrogen gas at a constant pressure of 700 mbar, measured using a digital manometer (2026P, Digitron). Polyether ether ketone capillary tubing (inner diameter, 75 μm) was connected via standard HPLC connectors and ferrules (Gilson Scientific Ltd.) to connect the input and exit ports of the T-junction block (Fig. S1*B*).

Microbubble Imaging Protocol and Imaging Equipment. Prepared microbubbles were transferred to glycerol coated coverslips and imaged. Initially, microbubbles were localized using brightfield and confocal microscopy using TCS SP5 (Leica Microsystems Ltd.) with a 488 nm excitation from an internal Argon ion laser through an 63× (N.A. 1.2) HCX PL APO CS water immersion objective lens with correction collar (11506279, Leica Microsystems Ltd.). Lifetime images were obtained using a TCSPC module (SPC830, Becker&Hickl) and internal FLIM detector (PMH-100, Becker&Hickl GmbH). The module was coupled and synchronized to the inverted scanning confocal microscope and Ti-Sapphire pulsed laser source (680–1,080 nm, 80 MHz, 140 fs, Chameleon Vision II, Coherent Inc.).

Two-photon excitation of microbubbles was performed at 800 nm and emission captured for lifetime/intensity at a band pass of 500–660 nm, and laser power was maintained <400 mW before entering the microscope to avoid bubble damage by intense irradiation (Movies S1 and S2). FLIM acquisition was continued until a pixel peak count of >100 was obtained, while the image format and analog-to-digital converter (ADC) were set to 256 × 256 and 256, respectively. FLIM data were exported and analyzed in TRI2 software (Version 2.4.1.1, Gray Institute for Radiation Oncology and Biology) (16) where a monoexponential model was fitted, using the Levenberg–Marquardt algorithm, to each pixel lifetime decay. Pixels were binned to maintain a minimum peak count of 100 counts per pixel and only lifetimes with reduced χ^2s $\chi_r^2 < 1.2$ were accepted in final images; thresholding was used to remove background noise. A false rainbow color scale was assigned to each fluorescence lifetime value (blue for a short lifetime and red for a long lifetime) to provide lifetime maps. Average microbubble lifetimes were calculated by masking the bubble of interest and fitting a monoexponential decay to all of the binned pixels (19). Further image analysis was completed by exporting fitted data to Origin Scientific solutions (OriginPro 8.5, OriginLab Corporation) and Matlab (R2009b, MathWorks Inc.) (Figs. S6 and S7).

To determine the optimal concentration of BODIPY-C_{10} in the lipid coating, we investigated bubbles prepared at [lipid]–[dye] ratios from 200:1–3,600:1. We did not detect any effect of dye concentration on measured viscosity or surface tension (Fig. S8) of lipid coating in this range.

Microbubble Acoustic Response Measurements and Setup. Microbubbles from the different DSPC+PEG ratio mixtures were prepared via sonication and fractionated by allowing them to stand at 4 °C for 3 h. Microbubbles were hydrodynamically isolated and streamed using a pair of coaxially aligned needles into the focal region of a pair of transducers (Fig. S5*A*). The microbubbles were interrogated by exciting the transmitting transducer (2.25 MHz focused, A306S, Panametrics-NDT) with a Gaussian-windowed five-cycle 2.25 MHz sinusoid pulse, generated by an arbitrary function generator (33220A, Agilent). The signal was then amplified (50 dB) by an rf power amplifier (325LA, Electric and Innovation) at a pulse repetition rate of 100 Hz. The scattered pressure was detected at 90° using a 3.5 MHz focused transducer (V382, Panametrics-NDT) where the signal was amplified (42 dB) using a pulser–receiver (DPR300, JSR Ultrasonics) and digitized with an oscilloscope (600 MHz, Xi64-A, Waverunner, LeCroy).

Syringe pumps (AL-1000, World Precision Instruments) were used to control the flow rates in the inner and outer needles of the coaxial flow. Deionized water was pumped through the outer needle (910 μm inner diameter), and the microbubble solution was delivered through the inner needle (190 μm inner diameter). A third syringe pump was used to maintain a stable flow by providing suction through a tube (2 mm inner diameter) located 2 cm away from the center of the inner needle. The transducers were aligned by maximizing the received backscatter from millimeter-sized air bubbles pumped through the inner needle. Precise alignment of the transducers and needles was achieved by separately mounting the components onto linear xyz manually adjustable stages. The transducers and coaxial flow were securely mounted into a degassed and deionized water tank. The incident pressure at the confocal region was measured using a calibrated 75 μm needle hydrophone (Precision Acoustics Ltd.), and the peak negative pressure was detected to be 284 kPa, which was comparable with medical ultrasound pressures (Fig. S5 *B* and *C*). Confirmation and evaluation of scattering events was performed by comparing the frequency spectrum from flow without microbubbles before each experiment. Microbubble flow was also visualized using a high-speed camera (Memrecam GX-8, NAC Image Technology) to confirm that microbubbles were isolated and that the inner flow was confined to a jet ∼100 μm in diameter traveling with a central line velocity of 0.12 ms^{-1}.

The scattered pressure from individual microbubbles was detected by capturing data only when a certain amplitude threshold had been exceeded. The stored data were transferred from the oscilloscope to a PC where they were analyzed using Matlab (v.11a, The MathWorks Inc.). The power Fourier transform for each signal was taken and summed within the 6 dB frequency bandwidth to obtain an estimate of the scattered power corresponding to the driving frequency. The scattered power depends not only on the viscosity of the microbubble coating but also on the effective elasticity (see below), as well as the size of an individual microbubble. In addition to the high-speed camera imaging, therefore, the size distributions of the different composition populations were determined before the scattering measurements to ensure they were matched as closely as possible. Optical images of the microbubbles were taken using brightfield light microscopy (DM500, Leica Microsystems Ltd.) with a 40× objective (0.8 N.A.) (LUMPLFLN 40XW, Olympus Corp.). The size distributions were subsequently determined using purpose-written code in Matlab (20). This provided an average Log-normal size distribution of 5.5 μm for all compositions ($n > 300$) (Fig. S5*D*). These data were used in theoretical simulations as described below to determine the expected sensitivity of the scattered pressure to the coating viscosity. Finally, the entire experiment was repeated three times, and the trend seen in this work was consistent.

Comparison of Theoretical Simulations of Microbubble Response to Experimental Results. Simulations were performed to determine the sensitivity of the microbubble acoustic response to the bubble size distribution and to variations in the coating characteristics. The theoretical results were then compared with those obtained experimentally. The response of a population of microbubbles having the same size distribution and driving pressure as measured in the experiment was simulated using a modified–Rayleigh–Plesset equation (Eq. **5**) describing encapsulated microbubbles with linear viscoelastic coatings characterized by parameters viscosity (μ_σ) and shear modulus (G_s) (21). This model was selected to maintain consistency with the calibration of the molecular rotor on the basis of shear viscosity. As discussed above, however, there is some uncertainty as to the relationship between macroscopic shear viscosity, as measured using conventional methods, and that determined by molecular rotors. It is appropriate, therefore, to consider μ_σ and G_s as effective viscosity and elasticity parameters rather than quantities that could be measured on a sample of the bulk coating material.

It is also important to note that Eq. **5** describes the microbubble coating as a thin shell and is valid for small amplitude oscillations. Alternative equations of motion, wherein viscous dissipation is described in terms of a 2D membrane dilatational viscosity, have also been proposed in the literature and are likely to be more appropriate for a surfactant monolayer (22, 23).

Since the results of this study and others have indicated that the microbubble coating may not be a simple monolayer, we elected to retain the linear viscoelastic shell treatment.

$$\ddot{R}R+\frac{3}{2}\dot{R}^2-\frac{P_0-P_L+P_i(t)}{\rho}-\frac{R}{\rho c}\dot{P}_L=0, \quad [5]$$

$$P_L=-4\mu_L\left(\frac{\dot{R}}{R}\right)-\Delta T_s+P_0\left(\frac{R_0}{R}\right)^{3\kappa}, \quad [6]$$

$$\Delta T_s=\frac{12ds}{R_0}\left(\frac{1}{1+x}\right)^4\left(G_s x+\mu_s\dot{x}\right), \quad [7]$$

$$x=\frac{R}{R_0}-1. \quad [8]$$

Eqs. **6–8** were solved using ODE45, an explicit fourth order Runge–Kutta algorithm, in Matlab (v.11a, The MathWorks Inc.) using a variable time step and parameter values (Table S1).

The mean shell viscosities measured in the experiments were used for μ_s, while the modulus was varied between 10 and 70 MPa. It was not possible to vary the effective elasticity independently of the coating viscosity or to measure it directly. It was assumed, however, that it would scale in a similar manner to viscosity as it is similarly dependent upon the surface molecular concentrations of the different coating components (23). The model was run for bubbles following the same size distributions as measured in the experiments (Fig. S5*D*) and the scattered power at the fundamental frequency (6 dB) plotted for comparison against experimental results (Fig. 2*D*). As may be seen, there was good agreement between the theoretical and experimental results, with large SDs in the data being produced by variations in either the bubble size and/or the coating parameters. This further demonstrates the advantage of using a direct measurement technique such as FLIM to measure coating parameters rather than relying on acoustic methods where the measured variable is dependent upon several parameters whose effects cannot readily be decoupled.

Further Lifetime Analysis of Individual Microbubble Lifetimes. When analyzing the lifetime data for individual microbubbles, we have detected heterogeneity in the lifetime distribution within shells. The analysis of the asymmetric histograms was simplified by extraction of the histogram lifetime data to Origin software (Origin Pro-8, Origin Lab). The peak fitting in Origin provided the justification for deciding on the color scheme in the FLIM images.

Two noncontacting DSPC microbubbles of a similar size. Two distinct Gaussian peaks are clearly apparent in Fig. 3*A*; therefore, no hidden peak fitting was required to assign the seismic color hue midpoint for the individual bubbles.

Single DSPC microbubble with heterogeneity within the lipid shell. The heterogeneity in the shell of a single DSPC bubble (Fig. 3*C*) showed some zonal differences that required further investigation, however the differences in lifetimes were not as obvious from the lifetime histogram as in Fig. 3*A*. However, by eye the lifetime histogram was asymmetric (Fig. S6), which suggested that there was more than one distinct population within the shell. Using a Gaussian fitting algorithm we confirmed that the histogram was indeed asymmetric (Fig. S6) and that two lifetime peaks were observed at 3.4 and 3.7 ns, corresponding to the distinct viscosities of 670 and 760 cP, respectively.

Multiple DSPC microbubbles in contact—touching bubbles. The multipeak analysis was applied to the lifetime histograms for bubbles 2 and 3 in Fig. 4*B*. For bubble 2 two peaks can be clearly seen, with maxima at 2.9 and 3.6 ns, which originate from two lifetime (viscosity) populations within that microbubble (Fig. S7*A*). Likewise, bubble 3, although less distinct, reveals two peaks within the lifetime histogram with maxima at 2.9 and 3.9 ns (Fig. S7*B*). Importantly, there is a common crossover space, between 3.1 and 3.4 ns, for these separate lifetime populations in bubbles 2 and 3 (Fig. S7). This common crossover space suggested to us that there are two very distinct regions of viscosity, corresponding to the lifetimes below 3.1 ns (lower viscosity) and those with lifetimes above 3.4 ns (higher viscosity). We applied the red/blue color hue (with separator at 3.1–3.4 ns) to the whole image in Fig. 4. It can be clearly seen that microbubble areas in contact with the neighboring bubbles appear as blue (lower viscosity, lifetimes below 3.1 ns), while areas of bubbles that are contact free are red (higher viscosity, lifetimes above 3.4 ns) (Fig. 4*A*). Despite the fact that domains of varied viscosity ranging between 300 and 1,200 cP were detected in this study, we note that it is possible that the rotor selectively avoids some lipid domains of extremely tight packing.

ACKNOWLEDGMENTS. The authors thank the Kick-Start scheme jointly funded by University College London and Imperial College London for supporting this work. M.K.K. thanks the Engineering and Physical Sciences Research Council for the Career Acceleration Fellowship (EP/E038980/1). E.S. thanks the Leverhulme Trust for supporting her research through the Philip Leverhulme Prize.

1. Lindner JR (2004) Microbubbles in medical imaging: Current applications and future directions. *Nat Rev Drug Discov* 3(6):527–532.
2. Stride E, Tang MX, Eckersley RJ (2009) Physical phenomena affecting quantitative imaging of ultrasound contrast agents. *Appl Acoust* 70(10):1352–1362.
3. Postema M, van Wamel A, Lancée CT, de Jong N (2004) Ultrasound-induced encapsulated microbubble phenomena. *Ultrasound Med Biol* 30(6):827–840.
4. Boudou T, et al. (2006) An extended modeling of the micropipette aspiration experiment for the characterization of the Young's modulus and Poisson's ratio of adherent thin biological samples: numerical and experimental studies. *J Biomech* 39(9):1677–1685.
5. Tang M-X, Eckersley RJ, Noble JA (2005) Pressure-dependent attenuation with microbubbles at low mechanical index. *Ultrasound Med Biol* 31(3):377–384.
6. Kooiman K, et al. (2010) Lipid distribution and viscosity of coated microbubbles. *Ultrasonics Symposium (IUS), 2010 IEEE* 900–903.
7. Sboros V, et al. (2007) Nanomechanical probing of microbubbles using the atomic force microscope. *Ultrasonics* 46(4):349–354.
8. de Jong N, Emmer M, van Wamel A, Versluis M (2009) Ultrasonic characterization of ultrasound contrast agents. *Med Biol Eng Comput* 47(8):861–873.
9. Kim DH, Klibanov AL, Needham D (2000) The influence of tiered layers of surface-grafted poly(ethylene glycol) on receptor–ligand-mediated adhesion between phospholipid monolayer-stabilized microbubbles and coated glass beads. *Langmuir* 16(6):2808–2817.
10. Borden MA, Longo ML (2002) Dissolution behavior of lipid monolayer-coated, air-filled microbubbles: Effect of lipid hydrophobic chain length. *Langmuir* 18(24):9225–9233.
11. Kim DH, Costello MJ, Duncan PB, Needham D (2003) Mechanical properties and microstructure of polycrystalline phospholipid monolayer shells: Novel solid microparticles. *Langmuir* 19(20):8455–8466.
12. Borden MA, et al. (2005) Influence of lipid shell physicochemical properties on ultrasound-induced microbubble destruction. *IEEE Trans Ultrason Ferroelectr Freq Control* 52(11):1992–2002.
13. Becker W, et al. (2004) Fluorescence lifetime imaging by time-correlated single-photon counting. *Microsc Res Tech* 63(1):58–66.
14. Kuimova MK, Yahioglu G, Levitt JA, Suhling K (2008) Molecular rotor measures viscosity of live cells via fluorescence lifetime imaging. *J Am Chem Soc* 130(21):6672–6673.
15. Förster T, Hoffmann G (1971) Viscosity dependence of fluorescent quantum yields of some dye systems. *Zeitschrift für Physikalische Chemie* 75(1-2):63–76.
16. Barber PR, et al. (2009) Multiphoton time-domain fluorescence lifetime imaging microscopy: Practical application to protein–protein interactions using global analysis. *J R Soc Interface* 6(Suppl 1):S93–S105.
17. Nipper ME, et al. (2008) Characterization of changes in the viscosity of lipid membranes with the molecular rotor FCVJ. *Biochim Biophys Acta* 1778(4):1148–1153.
18. Mohamedi G, et al. (2012) Effects of gold nanoparticles on the stability of microbubbles. *Langmuir* 28(39):13808–13815.
19. Hosny NA, Lee DA, Knight MM (2012) Single photon counting fluorescence lifetime detection of pericellular oxygen concentrations. *J Biomed Opt* 17(1):016007–016013.
20. Sennoga CA, et al. (2010) On sizing and counting of microbubbles using optical microscopy. *Ultrasound Med Biol* 36(12):2093–2096.
21. Hoff L (2001) *Acoustic Characterization of Contrast Agents for Medical Ultrasound Imaging* (Kluwer, Dordrecht, The Netherlands), pp xxi, 207.
22. Chatterjee D, Sarkar K (2003) A Newtonian rheological model for the interface of microbubble contrast agents. *Ultrasound Med Biol* 29(12):1749–1757.
23. Marmottant P, et al. (2005) A model for large amplitude oscillations of coated bubbles accounting for buckling and rupture. *J Acoust Soc Am* 118(6):3499–3505.